Total-Variation-Regularized Low-Rank Matrix Factorization for Hyperspectral Image Restoration

Wei He, *Student Member, IEEE*, Hongyan Zhang, *Member, IEEE*, Liangpei Zhang, *Senior Member, IEEE*, and Huanfeng Shen, *Senior Member, IEEE*

***Abstract*—In this paper, we present a spatial spectral hyperspectral image (HSI) mixed-noise removal method named total variation (TV)-regularized low-rank matrix factorization (LRTV). In general, HSIs are not only assumed to lie in a low-rank subspace from the spectral perspective but also assumed to be piecewise smooth in the spatial dimension. The proposed method integrates the nuclear norm, TV regularization, and L_1-norm together in a unified framework. The nuclear norm is used to exploit the spectral low-rank property, and the TV regularization is adopted to explore the spatial piecewise smooth structure of the HSI. At the same time, the sparse noise, which includes stripes, impulse noise, and dead pixels, is detected by the L_1-norm regularization. To tradeoff the nuclear norm and TV regularization and to further remove the Gaussian noise of the HSI, we also restrict the rank of the clean image to be no larger than the number of endmembers. A number of experiments were conducted in both simulated and real data conditions to illustrate the performance of the proposed LRTV method for HSI restoration.**

***Index Terms*—Hyperspectral image (HSI), low-rank matrix factorization, rank constraint, restoration, total variation (TV).**

I. INTRODUCTION

HYPERSPECTRAL image (HSI) data are acquired by high spectral resolution sensors, and consist of hundreds of contiguous narrow spectral band images. With the wealth of available spectral information, hyperspectral imagery has been found to be very useful for many remote sensing applications. However, hyperspectral imaging sensors unavoidably introduce noise into the acquired HSI data during the imaging process, which severely degrades the quality of the imagery and limits the precision of the subsequent processing, including classification [1], unmixing [2], [3], and target detection [4]. It is therefore an important preprocessing step to reduce the noise in hyperspectral imagery.

To date, many different HSI denoising methods have been proposed for the restoration of HSIs. HSI data contain hundreds of spectral channels, and each channel can be regarded as a gray-level image. On the other hand, each pixel can also be regarded as a 1-D signal. As a result, the simplest way is to utilize the traditional 2-D or 1-D denoising methods to reduce noise in the HSI band by band [5], [6] or pixel by pixel [7]. However, this kind of processing method ignores the correlations between different spectral bands or adjacent pixels and often results in a relatively low-quality result. In recent years, a number of algorithms have been proposed that combine the spatial and spectral information for HSI noise removal. Othman and Qian [8] proposed a hybrid spatial spectral derivative-domain wavelet shrinkage model, which benefits from the dissimilarity of the signal regularity in the spatial and spectral dimensions of the HSI. By treating the HSI as a 3-D multidimensional data cube, multidimensional Wiener filtering (MWF) [9], [10] and high-order rank-1 tensor decomposition [11], which jointly take into account the spatial spectral information, have also been adopted to denoise HSIs. In [12], the nonlocal similarity and spectral spatial structure of the hyperspectral imagery were introduced into a sparse representation framework. To sum up, all these spatial spectral methods have achieved comparable denoising results.

Total variation (TV) regularization is a powerful method in image processing. The TV-based algorithm is a very popular denoising approach because of its effectiveness in preserving edge information and the spatial piecewise smoothness [13], [14]. Apart from the image denoising processing field, TV regularization has been explored in many other image processing fields, e.g., superresolution [15], segmentation, and image reconstruction [16]. Recently, TV-based methods have also been extended to HSI restoration. In [17], a spatial spectral TV approach was used for HSI restoration. In [18], Kuiteing *et al.* proposed an iterative TV architecture for HSI reconstruction. Taking the spectral noise differences and the spatial information differences into consideration, Yuan *et al.* [19] proposed an HSI restoration algorithm employing a spectral spatial adaptive TV (SSAHTV) model. Despite their good performance in image processing, the TV-regularized methods still face some problems in impulse noise removal. Notably, TV regularization negatively affects the values of the pixels that are not impulse corrupted. To remedy this problem, two-phase methods have been considered for natural images in several papers [20], [21].

Manuscript received February 20, 2015; revised April 15, 2015 and May 28, 2015; accepted June 26, 2015. This work was supported in part by the National Basic Research Program of China (973 Program) under Grant 2011CB707105; by the National Natural Science Foundation of China under Grant 61201342 and Grant 41431175; and by the Fundamental Research Funds for Central Universities (2015904020202); and by the Key Laboratory of Mapping from Space, National Administration of Surveying, Mapping and Geoinformation. *(Corresponding author: Hongyan Zhang.)*

W. He, H. Zhang, and L. Zhang are with the State Key Laboratory of Information Engineering in Surveying, Mapping, and Remote Sensing and the Collaborative Innovation Center of Geospatial Technology, Wuhan University, Wuhan 430079, China (e-mail: zhanghongyan@whu.edu.cn).

H. Shen is with the School of Resource and Environmental Sciences and the Collaborative Innovation Center for Geospatial Technology, Wuhan University, Wuhan 430079, China.

Color versions of one or more of the figures in this paper are available online at http://ieeexplore.ieee.org.

Digital Object Identifier 10.1109/TGRS.2015.2452812

In these approaches, in the first phase, a median-type filter is used to identify the impulse-corrupted (sparse noise) pixel set, and in the second phase, the data-fidelity term of the model utilizes only the uncorrupted pixels to restore the corrupted image. A two-phase approach has also been used in HSI mixed-noise removal [22] and achieved comparable results.

In recent years, low-rank matrix factorization has been widely utilized as another powerful tool for image analysis, web search, and computer vision [23]–[25]. The low-rank model describes the problem of finding and exploiting low-dimensional structures in high-dimensional data. For an HSI, spectrally adjacent bands typically exhibit strong correlations, and spatially adjacent pixels in the HSI are also typically highly correlated, which both reveal the low-rank structure of hyperspectral imagery. Based on this fact, low-rank matrix factorization has recently been used in HSI denoising. One of the most famous traditional low-rank-based methods is principal component analysis (PCA) [26], which uses orthogonal transformation to convert the hyperspectral imagery into a set of linearly uncorrelated variables called principal components (PCs). Unfortunately, this classical method has two major drawbacks. First, it is sensitive to outliers; however, HSIs are often contaminated by outliers such as stripes, deadlines, impulse noise, and so on. Second, it mainly exploits the correlation between spectral bands, ignoring the spatial piecewise smoothness of local neighborhood pixels. In [23], Candès *et al.* solved the first problem and proposed the robust PCA (RPCA) model. They modeled the outliers as a sparse matrix and proved that, when the rank of the low-dimensional matrix and the distribution of the outlier matrix obey certain conditions, there is a high probability of recovering the low-rank matrix and the outlier matrix. This strategy has been successfully used in HSI mixed-noise removal [27]–[31] and has achieved state-of-the-art results. On the other hand, embedded in the spatial information, the low-rank model has been combined with other techniques to solve the second issue by simultaneously utilizing both the spectral and spatial information. In the method proposed in [32], PCA is first applied to the HSI, and the low-variance PCs are subsequently filtered by a 2-D bivariate wavelet shrinkage, and then by a 1-D dual-tree complex wavelet transformation, for each pixel. In [33], Zhao *et al.* exploited sparse coding to model the global redundancy and correlation (RAC) and the local RAC in the spectral domain and then used a low-rank constraint to deal with the global RAC in the spectral domain.

As we know, HSIs are often contaminated by several different types of noise, e.g., Gaussian noise, impulse noise, dead pixels, and stripes. In this paper, as in [27], we model impulse noise, dead pixels, and stripes as sparse noise, and we propose an HSI mixed-noise removal method by combining low-rank matrix factorization and TV regularization. From one aspect, the HSI is assumed to lie in a low-rank subspace, and the low-rank matrix factorization-based method can be used to efficiently separate the low-rank clean image and the sparse noise. Unfortunately, this model cannot effectively remove the heavy Gaussian noise because of the absence of an appropriate spatial constraint. In addition, as the intensity of the Gaussian noise increases, the effect of the low-rank and sparse matrix separation may be significantly degraded. From another aspect, the HSI is also assumed to be piecewise smooth in the spatial dimension, and the TV-based method can be adopted to effectively remove the Gaussian noise. These facts inspire us to integrate the low-rank model and the TV model. The low-rank model is used to capture the spectral correlations, and the TV regularization is utilized to capture the spatial piecewise smooth structure. It is worth mentioning that TV regularization combined with a low-rank constraint strategy has recently been utilized in HSI reconstruction [34] and fusion [35]. In this paper, we mainly focus on HSI mixed-noise removal. The main contributions of this paper are summarized as follows.

1) The low-rank matrix factorization model is studied and applied to HSI processing. From the Bayesian perspective, we also build up the relationship between the low-rank matrix factorization and the rank-constrained RPCA, which can be solved efficiently for HSI restoration.
2) TV regularization is incorporated in the low-rank matrix factorization model. The low-rank matrix factorization model is used to separate the clean spectral signal from the sparse noise, and the TV regularization is utilized to remove the Gaussian noise and enhance the spatial information.
3) The augmented Lagrange multiplier (ALM) [36]–[38] method is utilized and extended to solve the proposed model. The experimental results confirm that the proposed method clearly improves the restoration results, in comparison with some of the aforementioned techniques, in both the quantitative evaluation and the visual comparison.

The rest of this paper is organized as follows: In Section II, the TV model is studied and applied to HSI restoration. The TV-regularized low-rank matrix factorization (LRTV) model is introduced in Section III. In Section IV, both simulated and real data experiments are described and analyzed, and the conclusions are drawn in Section V.

II. TV MODEL FOR HSI RESTORATION

A. HSI Degradation Model

Observed HSI data that are contaminated by mixed noise, which are denoted by $\mathbf{Y} \in \mathbb{R}^{MN \times p}$, can be modeled as follows:

$$\mathbf{Y} = \mathbf{X} + \mathbf{S} + \mathbf{N} \tag{1}$$

where $\mathbf{Y} = [\mathbf{Y}_1, \mathbf{Y}_2, \ldots, \mathbf{Y}_p]$, $\mathbf{X} = [\mathbf{X}_1, \mathbf{X}_2, \ldots, \mathbf{X}_p]$, $\mathbf{S} = [\mathbf{S}_1, \mathbf{S}_2, \ldots, \mathbf{S}_p]$, and $\mathbf{N} = [\mathbf{N}_1, \mathbf{N}_2, \ldots, \mathbf{N}_p]$ are the Casorati matrices (a matrix whose columns comprise vectorized bands of the HSI) of the degraded HSI $u \in \mathbb{R}^{M \times N \times p}$, the clean image $f \in \mathbb{R}^{M \times N \times p}$, the sparse noise image $s \in \mathbb{R}^{M \times N \times p}$, and the Gaussian noise image $\mathcal{N} \in \mathbb{R}^{M \times N \times p}$, respectively. The purpose of HSI restoration is to estimate the clean image $\mathbf{X}$ from the noisy image $\mathbf{Y}$.

B. MAP Restoration Model

In recent years, the maximum *a posteriori* (MAP) estimation theory, which inherently includes prior constraints in the form of prior probability density functions, has been attracting attention and enjoying increasing popularity. It describes an ill-posed inverse problem and has been widely used in image processing [19]. Based on MAP estimation theory, the restoration model for an HSI can be described as the following constrained least squares problem:

$$\hat{\mathbf{X}} = \mathop{\arg\min}_{\mathbf{X}\in\mathbb{R}^{m\times n}} \left\{ \|\mathbf{Y}-\mathbf{X}\|_F^2 + \tau R(\mathbf{X}) \right\} \tag{2}$$

where $\mathbf{Y}$ and $\mathbf{X}$ are described as before; $\|\mathbf{Y}-\mathbf{X}\|_F^2$ is the data-fidelity term, which represents the distance between the observed noisy image $\mathbf{Y}$ and the original clear image $\mathbf{X}$; and $R(\mathbf{X})$ is the regularization term, which gives a prior model of the original clear HSI. τ is the regularization parameter used to balance the tradeoff between the fidelity term and the regularization term.

C. TV-Based HSI Restoration

The TV model was first proposed by Rudin *et al.* [39] to solve the gray-level image denoising problem because of its ability to effectively preserve edge information and promote piecewise smoothness. For a gray-level image x of size $M \times N$, the anisotropic TV norm [40] is defined as follows:

$$\begin{aligned} \|x\|_{\mathrm{TV}} = &\sum_{i=1}^{M-1}\sum_{j=1}^{N-1} \left\{ |x_{i,j}-x_{i+1,j}| + |x_{i,j}-x_{i,j+1}| \right\} \\ &+ \sum_{i=1}^{M-1} |x_{i,N}-x_{i+1,N}| + \sum_{j=1}^{N-1} |x_{M,j}-x_{M,j+1}|. \end{aligned} \tag{3}$$

It is easy to extend this gray-level TV norm to an HSI in a band-by-band manner. That is, every band of the HSI is treated as a gray-level image. The TV norm is then applied to each band, respectively, and then added together. This simple band-by-band HSI TV norm is defined as follows:

$$\|\mathbf{X}\|_{\mathrm{HTV}} = \sum_{j=1}^{p} \|\mathcal{F}\mathbf{X}_j\|_{\mathrm{TV}} \tag{4}$$

in which $\mathbf{X}_j$ represents the vector of the jth band of the HSI, and $\mathcal{F}:\mathbb{R}^{MN}\rightarrow\mathbb{R}^{M\times N}$ denotes the operator that reshapes the vector of the jth band back into the 2-D $M\times N$ image.

After defining the TV norm of the HSI, we can treat it as a prior and incorporate it in the MAP estimation (2). The HSI restoration model can then be written as follows:

$$\hat{\mathbf{X}} = \mathop{\arg\min}_{\mathbf{X}\in\mathbb{R}^{m\times n}} \left\{ \|\mathbf{Y}-\mathbf{X}\|_F^2 + \tau\|\mathbf{X}\|_{\mathrm{HTV}} \right\}. \tag{5}$$

For an HSI, it is often corrupted by mixed noise, including Gaussian noise and sparse noise. In this case, it is inappropriate to impose the data-fidelity term on all the space. If the sparse noise candidate set is denoted by Ω, then the TV-based HSI restoration model can be rewritten as follows [20]:

$$\hat{\mathbf{X}} = \mathop{\arg\min}_{\mathbf{X}\in\mathbb{R}^{m\times n}} \left\{ \|P_{\Omega^T}(\mathbf{Y}-\mathbf{X})\|_F^2 + \tau\|\mathbf{X}\|_{\mathrm{HTV}} \right\} \tag{6}$$

where Ω^T is the complementary space of Ω, and P_{Ω^T} is the orthogonal projector onto the span of the matrices vanishing in Ω.

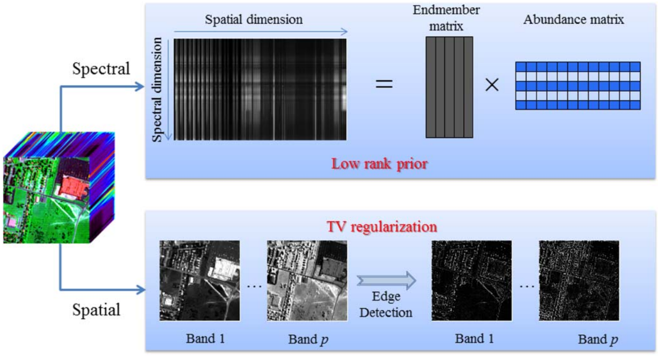

Fig. 1. Spatial and spectral perspectives of HSI data.

In addition, if we exactly know the sparse noise and denote it by $\mathbf{S}$, the TV model (6) can be written as follows:

$$\hat{\mathbf{X}} = \mathop{\arg\min}_{\mathbf{X}\in\mathbb{R}^{m\times n}} \left\{ \|\mathbf{Y}-\mathbf{X}-\mathbf{S}\|_F^2 + \tau\|\mathbf{X}\|_{\mathrm{HTV}} \right\}. \tag{7}$$

By carefully choosing the regularization parameter τ, model (7) is equal to the constrained TV model

$$\hat{\mathbf{X}} = \mathop{\arg\min}_{\mathbf{X}\in\mathbb{R}^{m\times n}} \|\mathbf{X}\|_{\mathrm{HTV}} \ \text{s.t.}\ \|\mathbf{Y}-\mathbf{X}-\mathbf{S}\|_F^2 \leq \varepsilon \tag{8}$$

in which ε represents the noise level of the Gaussian noise.

III. LRTV FOR HSI RESTORATION

In [27], it is well known that the low-rank-based method achieves an excellent sparse noise removal performance. However, as presented in [30], the method cannot completely remove Gaussian noise, which is independently distributed on each pixel of the HSI. Furthermore, when the sparse noise is structured, the sparse part may be treated as the low-rank part, significantly reducing the performance of the low-rank and sparse matrix separation. In this part, we incorporate the TV regularization into the low-rank matrix factorization-based HSI restoration model to explore the spatial piecewise smooth structure of the HSI, as presented in Fig. 1. Unlike the two-phase method proposed in [22], we combine the low-rank constraint and the TV regularization together in a unified mathematical framework and simultaneously detect the sparse noise and restore the HSI.

A. Low-Rank Matrix Factorization-Based HSI Restoration

As we know, HSI data are highly structured, i.e., the HSI lies in a low-dimensional space. From the perspective of the linear spectral mixing model, each spectral signature (row of $\mathbf{X}$) can be represented by a linear combination of a small number of pure spectral endmembers, as shown in Fig. 1. This inspires us to use the low-rank matrix factorization to model the HSI degradation as follows:

$$\mathbf{Y} = \mathbf{U}\mathbf{V} + \mathbf{S} + \mathbf{N} \tag{9}$$

in which $\mathbf{U}\in\mathbb{R}^{m\times r}$ represents the endmember matrix or "dictionary," $\mathbf{V}\in\mathbb{R}^{r\times n}$ can be regarded as the abundance or "coefficient" matrix, $\mathbf{U}\mathbf{V}$is the low-rank matrix factorization of the original clean image, and r is considered as the number of endmembers.

Next, we study the low-rank matrix factorization from a probabilistic perspective and build up the low-rank matrix factorization-based HSI restoration model. Differing from the linear spectral mixing model, in the low-rank matrix factorization model, we assume that $\mathbf{U}$ is a random dictionary. In addition, the coefficient values of the matrix $\mathbf{V}$ are also assumed to be randomly distributed. These assumptions have been adopted in probabilistic matrix factorization [41] and Bayesian RPCA [42].

Low-rank matrix factorization (9) has been widely used in image processing and analysis [24], [25]. In model (9), we assume that each element of $\mathbf{U} \in \mathbb{R}^{m\times r}, \mathbf{V} \in \mathbb{R}^{r\times n}$ is sampled from the Gaussian distribution, the sparse error $\mathbf{S}$ is sampled from the Laplace distribution, and the noise $\mathbf{G}$ obeys a Gaussian distribution. From the probabilistic view, we have the following:

$$\mathbf{U}_{ij} \sim \mathcal{N}\left(0, \lambda_u^{-1}\right) \tag{10}$$

$$\mathbf{V}_{ij} \sim \mathcal{N}\left(0, \lambda_v^{-1}\right) \tag{11}$$

$$\mathbf{S}_{ij} \sim \mathcal{L}\left(0, \lambda_s^{-1}\right) \tag{12}$$

$$\mathbf{G}_{ij} \sim \mathcal{N}\left(0, \lambda_g^{-1}\right). \tag{13}$$

By treating $\mathbf{U}$, $\mathbf{V}$, and $\mathbf{S}$ as model parameters, and λ_u, λ_v, λ_s, and λ_g as hyperparameters with fixed values, we use the Bayesian estimation to find $\mathbf{U}$, $\mathbf{V}$, and $\mathbf{S}$. From Bayes' rule, we have the following MAP formulation:

$$\begin{aligned} &p(\mathbf{U}, \mathbf{V}, \mathbf{S}|\mathbf{Y}, \lambda_u, \lambda_v, \lambda_s, \lambda_g) \\ &\qquad \propto p(\mathbf{Y}|\mathbf{U}, \mathbf{V}, \mathbf{S}, \lambda_g)p(\mathbf{U}|\lambda_u)p(\mathbf{V}|\lambda_v)p(\mathbf{S}|\lambda_s). \end{aligned} \tag{14}$$

Thus

$$\begin{aligned} \log p(\mathbf{U}, \mathbf{V}, \mathbf{S}|\mathbf{Y}, \lambda_u, \lambda_v, \lambda_s, \lambda_g) &= -\frac{\lambda_g}{2}\|\mathbf{Y} - \mathbf{U}\mathbf{V} - \mathbf{S}\|_F^2 \\ &\quad - \lambda_s\|\mathbf{S}\|_1 - \frac{\lambda_u}{2}\|\mathbf{U}\|_F^2 - \frac{\lambda_v}{2}\|\mathbf{V}\|_F^2 - C \end{aligned} \tag{15}$$

where C is a constant term independent of $\mathbf{U}$, $\mathbf{V}$, and $\mathbf{S}$. If we set $\lambda = \lambda_s/\lambda_g$, $\lambda'_u = \lambda_u/\lambda_g$, and $\lambda'_v = \lambda_v/\lambda_g$, then the MAP estimation is equivalent to the following restoration model:

$$\min_{\mathbf{U},\mathbf{V},\mathbf{S}} \frac{1}{2}\|\mathbf{Y} - \mathbf{U}\mathbf{V} - \mathbf{S}\|_F^2 + \lambda\|\mathbf{S}\|_1 + \frac{\lambda'_u}{2}\|\mathbf{U}\|_F^2 + \frac{\lambda'_v}{2}\|\mathbf{V}\|_F^2. \tag{16}$$

We can then further simplify the low-rank matrix factorization model (16) and deduce the rank-constrained RPCA model under certain conditions. First of all, we introduce a fact, which describes the relationship between the nuclear norm and the L_2-norm of the two factor matrices.

Lemma 1: For any matrix $\mathbf{X} \in \mathbb{R}^{m\times n}$, the following concept holds:

$$\|\mathbf{X}\|_* = \min_{\mathbf{U},\mathbf{V},\mathbf{L}=\mathbf{U}\mathbf{V}} \frac{1}{2}\left(\|\mathbf{U}\|_F^2 + \|\mathbf{V}\|_F^2\right).$$

If $\operatorname{rank}(\mathbf{X}) = r \le \min\{m, n\}$, then the aforementioned minimum is attained at a factor decomposition $\mathbf{X} = \mathbf{U}\mathbf{V}$, where $\mathbf{U} \in \mathbb{R}^{m\times r}$ and $\mathbf{V} \in \mathbb{R}^{r\times n}$.

The proof of Lemma 1 can be found in [43] and [44].

If we assume that $\lambda'_u = \lambda'_v = \lambda_2$ and the rank upper bound is r [i.e., $\mathbf{U} \in \mathbb{R}^{m\times r}$ and $\mathbf{V} \in \mathbb{R}^{r\times n}$ in (16)], then we can immediately deduce the following result using Lemma 1:

$$\begin{aligned} &\min_{\mathbf{U},\mathbf{V},\mathbf{S}} \frac{1}{2}\|\mathbf{Y} - \mathbf{U}\mathbf{V} - \mathbf{S}\|_F^2 + \lambda\|\mathbf{S}\|_1 + \frac{\lambda_2}{2}\|\mathbf{U}\|_F^2 + \frac{\lambda_2}{2}\|\mathbf{V}\|_F^2 \\ &\quad = \min_{\mathbf{U},\mathbf{V},\mathbf{S}} \frac{1}{2}\|\mathbf{Y} - \mathbf{U}\mathbf{V} - \mathbf{S}\|_F^2 + \lambda\|\mathbf{S}\|_1 + \lambda_2\left(\|\mathbf{U}\mathbf{V}\|_*\right) \\ &\quad = \min_{\mathbf{X},\mathbf{S},\operatorname{rank}(\mathbf{X})\le r} \frac{1}{2}\|\mathbf{Y} - \mathbf{X} - \mathbf{S}\|_F^2 + \lambda\|\mathbf{S}\|_1 + \lambda_2\left(\|\mathbf{X}\|_*\right). \end{aligned} \tag{17}$$

From (17), we can see that the low-rank matrix factorization restoration model (16) is the Lagrangian formalism of the rank-constrained RPCA model, which is presented as follows:

$$\min_{\mathbf{X},\mathbf{S}\in\mathbb{R}^{m\times n}} \|\mathbf{X}\|_* + \lambda\|\mathbf{S}\|_1 \text{ s.t. } \|\mathbf{Y} - \mathbf{X} - \mathbf{S}\|_F^2 \le \varepsilon, \operatorname{rank}(\mathbf{X}) \le r \tag{18}$$

in which ε represents the noise variance. Compared to the existing RPCA model [23], [27], it can be clearly observed that the constraint of the rank of the clean image being no larger than the number of endmembers is added in model (18). The rank of the matrix $\mathbf{X}$, which is an intrinsic feature of an HSI image, is very meaningful in the HSI restoration process. Unfortunately, in the case of the HSI being heavily corrupted by Gaussian noise, as the nuclear norm is just an approximation of the rank constraint, the minimizer of the RPCA model may not be low rank. By restricting the rank of the clean image to be no larger than the number of endmembers, model (18) can help to further remove the noise.

While the rank-constrained RPCA model (18) is nonconvex because of the inclusion of the rank constraint, it can be solved by the ALM-based method. More details about this issue can be found in [36]. On the other hand, model (18) can be deduced from the low-rank matrix factorization model (16). Therefore, the low-rank matrix factorization observation model (9) is used to describe the HSI degradation process, and the rank-constrained RPCA optimization model (18) is adopted to restore the HSI. In addition, we also call model (18) "low-rank matrix factorization" because of their equivalence.

B. LRTV for HSI Restoration

From the perspective of the low-rank matrix factorization model (18), it can perfectly decompose the observed image into the low-rank image and sparse noise image. However, unfortunately, it cannot efficiently remove heavy Gaussian noise because of the absence of an appropriate spatial constraint. Furthermore, this low-rank matrix factorization model can only separate the sparse noise from the observed image in the case of the locations of the sparse noise being randomly distributed [23]. That is, for HSI data, if the stripes are located in the same place in all the bands, the low-rank matrix factorization model (18) will fail to detect these stripes and will regard the sparse noise as the low-rank component. On the other hand, from the perspective of the TV model (8), it can significantly preserve the edge information and piecewise smooth structure. However, the spectral similarity is neglected, and the values or the locations of the sparse noise need to be predefined. All the aforementioned issues inspire us to integrate the two complementary models to restore the HSI. We can then carry out the following LRTV restoration model:

$$\min_{\mathbf{X},\mathbf{S}\in\mathbb{R}^{m\times n}} \|\mathbf{X}\|_* + \tau\|\mathbf{X}\|_{\mathrm{HTV}} + \lambda\|\mathbf{S}\|_1 \quad \text{s.t.} \quad \|\mathbf{Y}-\mathbf{X}-\mathbf{S}\|_F^2 \le \varepsilon, \quad \mathrm{rank}(\mathbf{X}) \le r \tag{19}$$

where τ is the parameter used to control the tradeoff between the nuclear norm and the TV norm, and λ is the parameter used to restrict the sparsity of the sparse noise. In the LRTV model, when τ is set to zero, the optimization (19) is degraded into a low-rank matrix regularization model (18).

The LRTV model (19) can simultaneously capture the spatial and spectral information of the HSI. The low-rank constraint can make use of the spectral similarity of all the pixels and can provide the sparse noise information when combined with the sparsity constraint. After the sparse noise is confirmed, the TV regularization can be used to capture the spatial information and enhance the piecewise smooth structure of each band and, as a result, promote the removal of the Gaussian noise. This will, in return, help to decompose the low-rank image and the sparse noise. As the iteration progresses, we progressively separate the sparse noise from the observed image and obtain a restored image with the spectral structure of spectral similarity and the spatial structure of piecewise smoothness.

C. Optimization Procedure

The optimization problem (19) can be solved by various methods. For efficiency, we adopt the ALM [36] method in this paper. We first convert (19) to the following equivalent problem:

$$\min_{\mathbf{L},\mathbf{X},\mathbf{S}\in\mathbb{R}^{m\times n}} \|\mathbf{L}\|_* + \tau\|\mathbf{X}\|_{\mathrm{HTV}} + \lambda\|\mathbf{S}\|_1 \quad \text{s.t.} \quad \|\mathbf{Y}-\mathbf{L}-\mathbf{S}\|_F^2 \le \varepsilon, \quad \mathrm{rank}(\mathbf{L}) \le r, \quad \mathbf{L}=\mathbf{X}. \tag{20}$$

This problem can be solved by the ALM method, which minimizes the following augmented Lagrangian function:

$$\begin{aligned}\min \ell(\mathbf{L},\mathbf{X},\mathbf{S},\Lambda_1,\Lambda_2) = &\min_{\mathbf{X},\mathbf{S},\mathbf{L},\Lambda_1,\Lambda_2} \|\mathbf{L}\|_* + \tau\|\mathbf{X}\|_{\mathrm{HTV}} + \lambda\|\mathbf{S}\|_1\\ &+ \langle\Lambda_1,\mathbf{Y}-\mathbf{L}-\mathbf{S}\rangle + \langle\Lambda_2,\mathbf{X}-\mathbf{L}\rangle\\ &+ \frac{\mu}{2}\left(\|\mathbf{Y}-\mathbf{L}-\mathbf{S}\|_F^2 + \|\mathbf{X}-\mathbf{L}\|_F^2\right)\\ &\text{s.t.} \quad \mathrm{rank}(\mathbf{L}) \le r\end{aligned} \tag{21}$$

where μ is the penalty parameter, and Λ_1 and $\Lambda_2$are the Lagrange multipliers.

A natural way to solve the problem is to iteratively optimize the augmented Lagrangian function (21) over one variable, while fixing the others. Specifically, in the $k+1$th iteration, we update the variables as follows:

$$\mathbf{L}^{(k+1)} = \arg\min_{\mathrm{rank}(\mathbf{L})\le r} \ell\left(\mathbf{L},\mathbf{X}^{(k)},\mathbf{S}^{(k)},\Lambda_1^{(k)},\Lambda_2^{(k)}\right) \tag{22a}$$

$$\mathbf{X}^{(k+1)} = \arg\min_{\mathbf{X}} \ell\left(\mathbf{L}^{(k+1)},\mathbf{X},\mathbf{S}^{(k)},\Lambda_1^{(k)},\Lambda_2^{(k)}\right) \tag{22b}$$

$$\mathbf{S}^{(k+1)} = \arg\min_{\mathbf{S}} \ell\left(\mathbf{L}^{(k+1)},\mathbf{X}^{(k+1)},\mathbf{S},\Lambda_1^{(k)},\Lambda_2^{(k)}\right) \tag{22c}$$

$$\Lambda_1^{(k+1)} = \Lambda_1^{(k)} + \mu\left(\mathbf{Y}-\mathbf{L}^{(k+1)}-\mathbf{S}^{(k+1)}\right) \tag{22d}$$

$$\Lambda_2^{(k+1)} = \Lambda_2^{(k)} + \mu\left(\mathbf{X}^{(k+1)}-\mathbf{L}^{(k+1)}\right). \tag{22e}$$

The optimization problem is now divided into three major subproblems presented in (22a)–(22c). For (22a), we can deduce that

$$\begin{aligned}\mathbf{L}^{(k+1)} &= \arg\min_{\mathrm{rank}(\mathbf{L})\le r} \ell\left(\mathbf{L},\mathbf{X}^{(k)},\mathbf{S}^{(k)},\Lambda_1^{(k)},\Lambda_2^{(k)}\right)\\ &= \arg\min_{\mathrm{rank}(\mathbf{L})\le r} \|\mathbf{L}\|_* + \left\langle\Lambda_1^{(k)},\mathbf{Y}-\mathbf{L}-\mathbf{S}^{(k)}\right\rangle + \left\langle\Lambda_2^{(k)},\mathbf{X}^{(k)}-\mathbf{L}\right\rangle\\ &\quad + \frac{\mu}{2}\left(\left\|\mathbf{Y}-\mathbf{L}-\mathbf{S}^{(k)}\right\|_F^2 + \left\|\mathbf{X}^{(k)}-\mathbf{L}\right\|_F^2\right)\\ &= \arg\min_{\mathrm{rank}(\mathbf{L})\le r} \|\mathbf{L}\|_* + \mu\left\|\mathbf{L}-\frac{1}{2}\left(\mathbf{Y}+\mathbf{X}^{(k)}-\mathbf{S}^{(k)} + \left(\Lambda_1^{(k)}+\Lambda_2^{(k)}\right)/\mu\right)\right\|_F^2.\end{aligned} \tag{23}$$

The step for updating $\mathbf{L}$ can be solved by the following Lemma 2.

Lemma 2 [45]: Let $\mathbf{W}\in\mathbb{R}^{MN\times p}$ be a given matrix, then the singular value decomposition (SVD) of a matrix $\mathbf{W}$ of rank r is defined as follows:

$$\mathbf{W} = UE_rV^*,\ E_r = \mathrm{diag}\left(\{\sigma_i\}_{1\le i\le r}\right). \tag{24}$$

The singular value shrinkage operator then obeys

$$D_\delta(\mathbf{W}) = \arg\min_{\mathrm{rank}(\mathbf{L})\le r} \delta\|\mathbf{L}\|_* + \frac{1}{2}\|\mathbf{L}-\mathbf{W}\|_F^2 \tag{25}$$

where

$$D_\delta(\mathbf{W}) = UD_\delta(E_r)V^*,\ D_\delta(E_r) = \mathrm{diag}\left\{\max\left((\sigma_i-\delta),0\right)\right\}.$$

By using Lemma 2, we can easily obtain the following optimization result of (23):

$$\mathbf{L}^{(k+1)} = D_{\frac{1}{(2\mu)}}\left(\frac{1}{2}\left(\mathbf{Y}+\mathbf{X}^{(k)}-\mathbf{S}^{(k)}+\left(\Lambda_1^{(k)}+\Lambda_2^{(k)}\right)/\mu\right)\right). \tag{26}$$

As to subproblem (22b), we have the following:

$$\begin{aligned}\mathbf{X}^{(k+1)} &= \arg\min_{\mathbf{X}} \ell\left(\mathbf{L}^{(k+1)},\mathbf{X},\mathbf{S}^{(k)},\Lambda_1^{(k)},\Lambda_2^{(k)}\right)\\ &= \arg\min_{\mathbf{X}} \tau\|\mathbf{X}\|_{\mathrm{HTV}} + \left\langle\Lambda_2^{(k)},\mathbf{X}-\mathbf{L}^{(k+1)}\right\rangle\\ &\quad + \frac{\mu}{2}\left\|\mathbf{X}-\mathbf{L}^{(k+1)}\right\|_F^2\\ &= \arg\min_{\mathbf{X}} \tau\|\mathbf{X}\|_{\mathrm{HTV}} + \frac{\mu}{2}\left\|\mathbf{X}-\mathbf{L}^{(k+1)}+\frac{\Lambda_2^{(k)}}{\mu}\right\|_F^2.\end{aligned} \tag{27}$$

We define $Q=\mathbf{L}^{(k+1)}-(\Lambda_2^{(k)}/\mu)$ and $Q=[Q_1,Q_2,\ldots,Q_p]\in\mathbb{R}^{MN\times p}$, where optimization (27) can be split into p

subproblems, and each subproblem is to solve

$$\mathbf{X}_j^{(k+1)} = \arg\min_{\mathbf{X}_j} \frac{\tau}{\mu}\|\mathbf{H}\mathbf{X}_j\|_{\mathrm{TV}} + \frac{1}{2}\|\mathbf{X}_j - Q_j\|^2. \tag{28}$$

In this paper, we use the fast gradient-based algorithm introduced in [40] to solve (28). For the third subproblem (22c), we have the following:

$$\begin{aligned}\mathbf{S}^{(k+1)} &= \arg\min_{\mathbf{S}} \ell\left(\mathbf{L}^{(k+1)}, \mathbf{X}^{(k+1)}, \mathbf{S}, \Lambda_1^{(k)}, \Lambda_2^{(k)}\right)\\ &= \arg\min_{\mathbf{S}} \lambda\|\mathbf{S}\|_1 + \left\langle \Lambda_1^{(k)}, \mathbf{Y} - \mathbf{L}^{(k+1)} - \mathbf{S}\right\rangle\\ &\quad + \frac{\mu}{2}\left\|\mathbf{Y} - \mathbf{L}^{(k+1)} - \mathbf{S}\right\|_F^2\\ &= \arg\min_{\mathbf{S}} \lambda\|\mathbf{S}\|_1 + \frac{\mu}{2}\left\|\mathbf{S} - \left(\mathbf{Y} - \mathbf{L}^{(k+1)} + \frac{\Lambda_1^{(k)}}{\mu}\right)\right\|_F^2.\end{aligned} \tag{29}$$

By introducing the following soft-thresholding (shrinkage) operator:

$$\Re_\Delta(x) = \begin{cases} x - \Delta, & \text{if } x > \Delta\\ x + \Delta, & \text{if } x > \Delta\\ 0, & \text{otherwise}\end{cases} \tag{30}$$

where $x \in \mathbb{R}$ and $\Delta > 0$, the optimization of (29) can be expressed as follows:

$$\mathbf{S}^{(k+1)} = \Re_{\frac{\lambda}{\mu}}\left(\mathbf{Y} - \mathbf{L}^{(k+1)} + \frac{\Lambda_1^{(k)}}{\mu}\right). \tag{31}$$

Summarizing the aforementioned description, we arrive at an augmented Lagrangian alternating direction method to solve the LRTV model, as presented in Algorithm 1.

Algorithm 1 LRTV solver

```
Input: $MN \times p$ matrix $\mathbf{Y}$, desired rank $r$, stopping criteria
    $\varepsilon_1$ and $\varepsilon_2$, and regularized parameters $\tau$ and $\lambda$
Output: Restored image $\mathbf{X}$
Initialize: $\mathbf{L}=\mathbf{X}=\mathbf{S}=0$, $\Lambda_1=\Lambda_2=0$, $\mu=10^{-2}$, $\mu_{\max}=10^6$,
    $\rho = 1.5$ and $k = 0$
Repeat until convergence
    Update $\mathbf{L}^{(k+1)}$, $\mathbf{X}^{(k+1)}$, $\mathbf{S}^{(k+1)}$, $\Lambda_1^{(k+1)}$, and $\Lambda_2^{(k+1)}$ via (22)
    Update the parameter $\mu := \min(\rho\mu, \mu_{\max})$
    Check the convergence conditions
$\|\mathbf{Y}-\mathbf{L}^{(k+1)}-\mathbf{S}^{(k+1)}\|_F/\|\mathbf{Y}\|_F \le \varepsilon_1$ and $\|\mathbf{L}^{(k+1)}-\mathbf{X}^{(k+1)}\|_\infty \le \varepsilon_2$
```

In the LRTV solver, the inputs are the noisy image $\mathbf{Y} \in \mathbb{R}^{MN\times p}$, the desired rank r, the stopping criteria ε_1 and ε_2, and the regularized parameters τ and λ. The output is the clean image $\mathbf{X} \in \mathbb{R}^{MN\times p}$. In addition, the initializations of the variables are important. As in [37], we initialize $\mathbf{L} = \mathbf{X} = \mathbf{S} = 0$, $\Lambda_1 = \Lambda_2 = 0$. For variable μ shown in the augmented Lagrangian function (21), we initialize it as 10^{-2} and update it as $\mu := \min(\rho\mu, \mu_{\max})$ in each iteration step. This strategy of determining the variable μ has been widely used in the ALM-based methods, which can support the convergence of the algorithm [36], [37], [46].

D. *Parameter Determination*

As presented in Algorithm 1, the desired rank r, the stopping criteria ε_1 and ε_2, and the regularized parameters τ and λ need to be determined as prior knowledge. In all the experiments, we set $\lambda = 1/\sqrt{MN}$ and $\varepsilon_1 = \varepsilon_2 = 10^{-8}$. What we need to discuss is the desired rank r and the regularized parameter τ.

The desired rank r represents the number of endmembers in the HSI. Unfortunately, it is not easy to directly obtain the number of endmembers in real HSI processing. In this case, we resort to the HSI subspace identification method called HySime, as proposed in [47], to estimate the number of endmembers.

The regularized parameter τ is used to control the tradeoff between the nuclear norm and the TV norm. When τ is set to zero, the optimization (19) is degraded into the low-rank matrix regularization model (18). From (28), it seems that the TV regularization is mainly influenced by the value of τ/μ. However, as the iteration progresses in the LRTV solver, $\tau/\mu \to 0$ as $\mu \to +\infty$. That is, the role of the TV regularization is getting smaller. As a result, τ has a slight relationship with the initial value of μ. In the experiments, we set $\tau = 0.01$.

IV. EXPERIMENTAL RESULTS AND DISCUSSION

Both simulated and real image data experiments were undertaken to demonstrate the effectiveness of the LRTV method for HSI restoration. To thoroughly evaluate the performance of the proposed algorithm, we selected two different noise removal methods for comparison, i.e., the SSAHTV model [19] and the low-rank matrix recovery (LRMR) model [27]. SSAHTV is one of the state-of-the-art TV-based HSI restoration methods, and LRMR is a state-of-the-art low-rank-based method. In all the simulated experiments, the parameters in SSAHTV and LRMR were manually adjusted to the optimal. In the real data experiments, we first resorted to the parameter selection methods in [19] and [27], and we then fine tuned the parameters and chose the ones that corresponded to the best visual results. In addition, the gray values of each HSI band were normalized to [0, 1], as in [19] and [27].

A. *Simulated Data Experiments for Mixed-Noise Removal*

The synthetic data were generated using the ground truth of the Indian Pines data set [48], and the spectral signatures were extracted from the USGS digital spectral library [49]. We assigned the pixels of the same label with a specific signature from the spectral library. All the unlabeled pixels were also replaced by the same signature. In total, we replaced 16 classes of labeled pixels and all the unlabeled pixels with the 17th signature from the spectral library. The size of the synthetic image was $145 \times 145 \times 224$. The reflectance values of all the voxels in the HSI were linearly mapped to [0, 1]. The synthetic HSI data can be considered as clean data [12].

To simulate a noisy image, we added Gaussian noise and salt-and-pepper impulse noise to all the bands of the simulated clean HSI, as the following two cases:

Case 1) For different bands, the noise intensity was equal. In this case, the same distribution of zero-mean Gaussian noise and the same percentage of impulse

TABLE I
QUANTITATIVE EVALUATION OF THE DIFFERENT RESTORATION ALGORITHMS WITH THE SIMULATED DATA IN CASE 1

Noise variance	Evaluation index	SSAHTV	RPCA-SSAHTV	LRMR	LRTV
G=0.025 P=0.05	MPSNR (dB)	29.34	39.89	<u>43.73</u>	**47.26**
	MSSIM	0.9216	<u>0.9965</u>	0.9904	**0.9984**
	MSA	3.1177	0.7779	<u>0.6465</u>	**0.2710**
G=0.050 P=0.10	MPSNR (dB)	25.50	35.81	<u>38.89</u>	**41.63**
	MSSIM	0.8814	<u>0.9921</u>	0.9722	**0.9942**
	MSA	4.8130	1.3683	<u>1.0634</u>	**0.6304**
G=0.075 P=0.15	MPSNR (dB)	23.73	32.92	<u>34.44</u>	**39.12**
	MSSIM	0.8207	<u>0.9655</u>	0.9282	**0.9879**
	MSA	6.1168	1.9602	<u>1.8662</u>	**0.9660**
G=0.100 P=0.20	MPSNR (dB)	22.24	30.73	<u>31.69</u>	**36.52**
	MSSIM	0.7384	<u>0.9472</u>	0.8892	**0.9787**
	MSA	7.4864	2.5327	<u>2.4969</u>	**1.2833**

noise were added to each band. The variances of the Gaussian noise were $G = 0.025$, 0.05, 0.075, and 0.1, respectively, and the percentages of the impulse noise were $P = 0.05$, 0.1, 0.15, and 0.2, respectively.

Case 2) For different bands, the noise intensity was different. In this case, different variance zero-mean Gaussian noise was added to each band, with the variance value being randomly selected from 0 to 0.2, and different percentages of impulse noise were added, which were randomly selected from 0 to 0.2. In the simulated experiments, as the SSAHTV method does not remove impulse noise, we first used RPCA to filter the impulse noise, and then, SSAHTV was applied to the low-rank part of the RPCA model. We denote this restoration method as RPCA-SSAHTV. After restoring the image, the peak signal-to-noise ratio (PSNR) index and the structural similarity (SSIM) index [50] were adopted to give a quantitative assessment for the results of the simulated image experiments. For the HSI, we computed the PSNR and SSIM values, between each noise-free band and denoised band, and then averaged them. These metrics are denoted as MPSNR (mean PSNR) and MSSIM (mean SSIM). In order to evaluate the spectral fidelity of the denoising result, the mean spectral angle (MSA) index was also used.

The restoration results of the different algorithms for the synthetic HSI data in Case 1 are presented in Table I. The best results for each quality index are labeled in bold, and the second-best results for each quality index are underlined. Here, it is clear that the proposed method provides the highest values in both MPSNR and MSSIM and the lowest MSA, which confirms the advantage of the proposed method over the other methods.

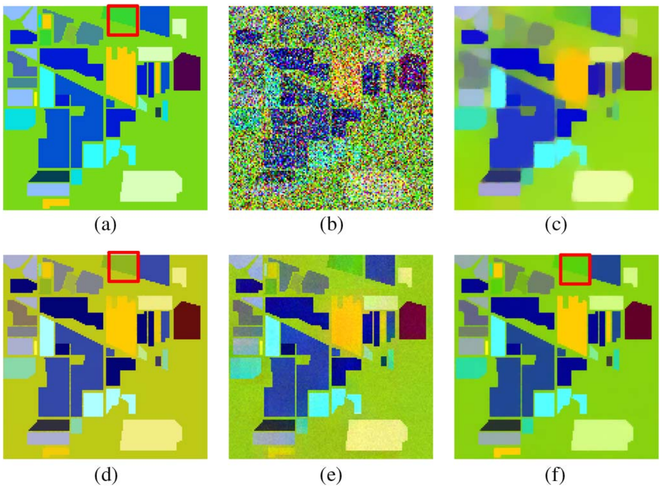
(a) (b) (c) (d) (e) (f)

Fig. 2. Restoration results in the simulated experiments in Case 2. (a) Original false-color image (R: 6, G: 88, B: 221). (b) Noisy band. (c) SSAHTV. (d) RPCA-SSAHTV. (e) LRMR. (f) LRTV.

TABLE II
QUANTITATIVE EVALUATION OF THE DIFFERENT RESTORATION ALGORITHMS WITH THE SIMULATED DATA IN CASE 2

Evaluation index	SSAHTV	RPCA-SSAHTV	LRMR	LRTV
MPSNR (dB)	22.31	31.01	<u>31.23</u>	**36.35**
MSSIM	0.7985	<u>0.9485</u>	0.8867	**0.9791**
MSA	7.0395	2.8912	<u>2.7439</u>	**1.4995**

For Case 2, we first present some typical bands of the synthetic HSI data before and after restoration. Fig. 2 shows the false-color composite of the synthetic image. By comparing the restoration results of the four different methods, it can be clearly seen that LRTV performs best, effectively suppressing the noise while preserving the spectral information. SSAHTV introduces artifacts, and the restored image is blurred. LRMR can more or less remove the noise and preserve the spectral information, but the removal of the Gaussian noise is not complete. The result of RPCA-SSAHTV perfectly preserves the spatial structure of the image. This is mainly because the impulse noise is filtered by RPCA, and the spatial information is fully restored by the TV-based method. However, the major disadvantage of this method is that the spectral deformation is serious, e.g., as shown in the red rectangles in Fig. 2(d) and (f). The advantages and disadvantages of RPCA-SSAHTV are indicated in Table II, which presents the quantitative assessment of all the restoration results. In Table II, the MSSIM value of RPCA-SSAHTV is comparable to that of LRTV, which is due to the fact that the SSIM is a quality assessment measure based on the degradation of the structural information. However, the MPSNR value of the RPCA-SSAHTV results is even lower than that of LRMR. As to the MSA values, which suggest the extent of the spectral distortion, the results of the RPCA-SSAHTV and LRMR methods are comparable, they are much better than the results of SSAHTV, and they are significantly inferior to the results of the LRTV method. On the whole, the experimental results of LRTV are the best, in both the visual assessment in Fig. 2 and the quantitative assessment in Table II. This is mainly because LRTV employs structural information in the TV regularization and the spectral similarity in the low-rank constraint. We also show the PSNR and SSIM values of each band in the Case 2 experiment in Fig. 3. Here, LRTV achieves the best PSNR and SSIM values in almost all the bands, further indicating that the proposed method outperforms the other methods in HSI restoration.

To further compare the performances of all the restoration algorithms, we also show the spectral signatures before and after restoration. Fig. 4 shows the spectral signatures of pixel (100, 100). Combined with the quantitative assessment of the MSA

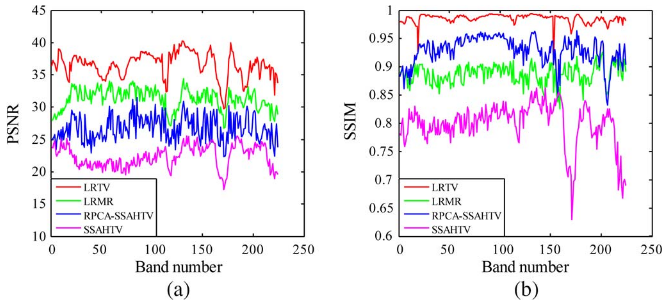

(a) (b)

Fig. 3. PSNR and SSIM values of each band of the experimental results in Case 2. (a) PSNR values. (b) SSIM values.

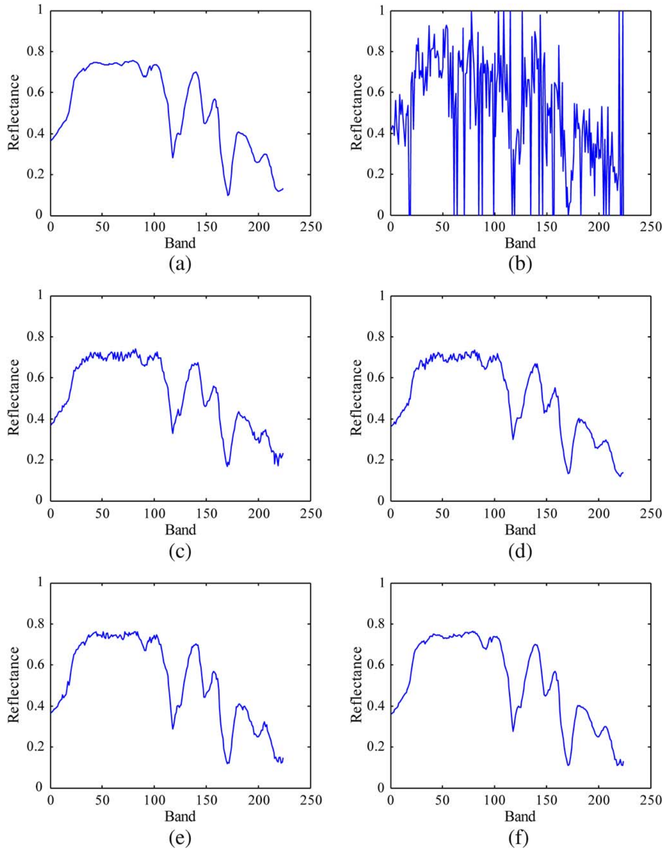

(a) (b) (c) (d) (e) (f)

Fig. 4. Spectrum of pixel (100, 100) in the restoration results: (a) original, (b) noisy, (c) SSAHTV, (d) RPCA-SSAHTV, (e) LRMR, and (f) LRTV.

values presented in Tables I and II, it can be clearly seen that the proposed LRTV method produces the best spectral signature.

B. Real Data Experiments

Three real-world HSI data sets were also used in our experiments: the Hyperspectral Digital Imagery Collection Experiment (HYDICE) urban data set, the Airborne Visible/Infrared Imaging Spectrometer (AVIRIS) Indian Pines data set, and an Earth Observing-1 (EO-1) Hyperion data set. Before the restoration process, the gray values of each HSI band were normalized to [0, 1]. In the real data experiment, SSAHTV performed similarly to the RPCA-SSAHTV method because the impulse noise was not so serious in the real-world image. Therefore, only SSAHTV and LRMR were adopted as comparison methods.

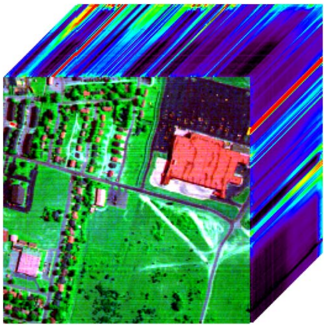

Fig. 5. HYDICE urban data set used in real data experiment 1.

1) HYDICE Urban Data Set: The HYDICE urban image can be downloaded online at [51]. The original image is $307 \times 307 \times 210$ in size, and we selected a subimage of size $200 \times 200 \times 210$ for our experiment. The urban image presented in Fig. 5 is polluted by stripes, deadlines, the atmosphere, water absorption, and other unknown noise. In this first real data experiment, for LRMR, the parameters were set as $r = 4$ and $k = 4000$. For the SSAHTV method, the regularization parameter was set to 3.

Figs. 6 and 7 present bands 103 and 206 of the restored images. From the results, we can see that the SSAHTV method can more or less remove the stripes, but it causes the restored results to be oversmooth. In addition, some local details are distorted, as shown in Fig. 7. LRMR cannot effectively remove the stripes in Fig. 7. This is mainly because of the fact that the stripes exist in the same place from bands 199 to 210. That is, in the low-rank and sparse decomposition, the stripes are regarded as the low-rank part, which is assumed to be the clean image. Compared to LRMR, LRTV uses the TV regularization to mine the spatial information and can significantly reduce this kind of stripes. Overall, the results show that LRTV performs best.

Fig. 8 shows the horizontal mean profiles of band 206 before and after restoration. The horizontal axis in Fig. 8 represents the row number, and the vertical axis represents the mean digital number value of each row. As shown in Fig. 8(a), due to the existence of mixed noise, there are rapid fluctuations in the curve. After the restoration processing, the fluctuations are more or less suppressed. Here, the LRTV method appears to perform best. This is in accordance with the visual results presented in Fig. 7, which show that LRMR fails to restore most of the stripes. In Fig. 8, SSAHTV achieves comparable results to LRTV. However, we suspect that the result of SSAHTV is oversmooth, as deduced from the performance in Fig. 7(b).

2) AVIRIS Indian Pines Data Set: The Indian Pines data set [48] was used in the second experiment. This data set was acquired by the NASA AVIRIS instrument over the Indian Pines test site in Northwestern Indiana in 1992, and the size is 145×145 pixels and 220 bands. Fig. 9 shows the color image by combining bands 3, 147, and 219. In this real data experiment, the parameters of LRMR were set as $r = 5$ and $k = 4000$. The regularization parameter λ of SSAHTV was set to 3.

The Indian Pines data set is mainly corrupted by the atmosphere and water absorption. The first few bands and the last few bands are also seriously polluted by Gaussian noise and impulse noise. Figs. 10 and 11 present the restoration results of

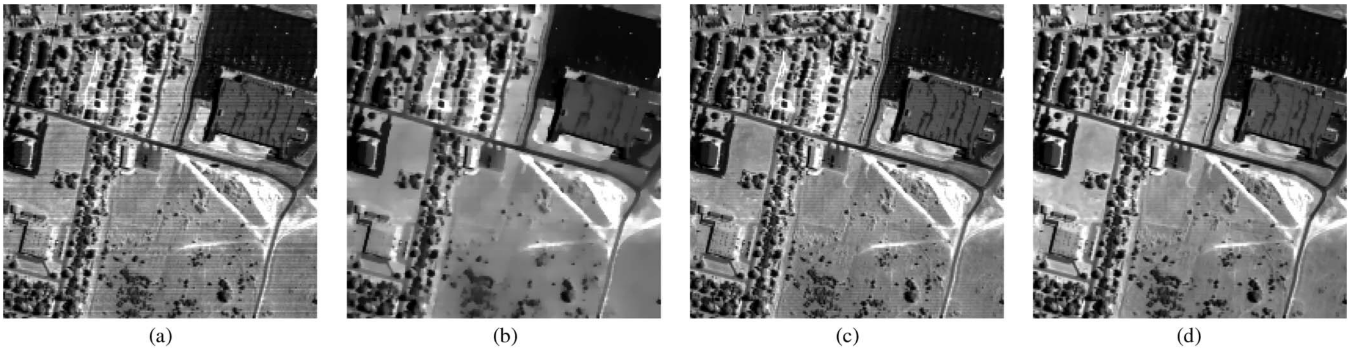

Fig. 6. Restoration results of band 103 in real data experiment 1. (a) Original. (b) SSAHTV. (c) LRMR. (d) LRTV.

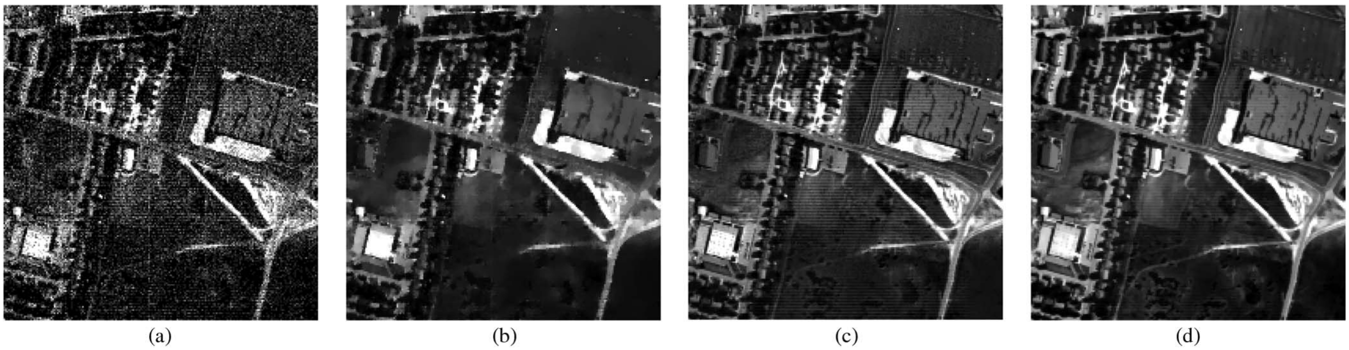

Fig. 7. Restoration results of band 206 in real data experiment 1. (a) Original. (b) SSAHTV. (c) LRMR. (d) LRTV.

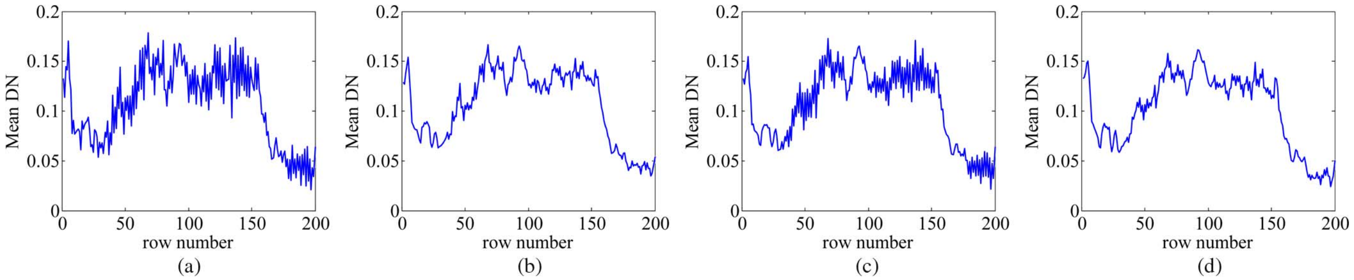

Fig. 8. Horizontal mean profiles of band 206 in real data experiment 1. (a) Original. (b) SSAHTV. (c) LRMR. (d) LRTV.

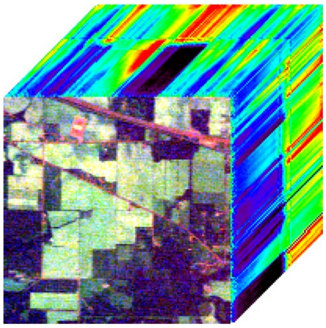

Fig. 9. AVIRIS Indian Pines data set used in real data experiment 2.

bands 1 and 220 by the different restoration methods. Here, it can be clearly observed that SSAHTV fails to restore the image, as it is not suitable for the removal of heavy impulse noise. LRMR can remove some of the noise, but some dense noise still exists in the restored result. LRTV performs best, effectively suppressing the Gaussian noise and simultaneously keeping the local details and structural information of the image.

3) EO-1 Hyperion Data Set: The third real data experiment adopted an EO-1 Hyperion image as the test image [52]. The original image was $400 \times 1000 \times 242$ in size, and a subset of size $200 \times 200 \times 166$ was used after the removal of water absorption bands. The image is shown in Fig. 12. In the experiment, the parameters of LRMR were set as $r = 6$ and $k = 4000$. For the SSAHTV method, the regularization parameter was set to 3.

This Hyperion data set is mainly corrupted by stripes and deadlines. We display the restoration results of band 1 and band 156 in Figs. 13 and 14, respectively. From the visual results presented in Figs. 13 and 14, it can be clearly observed that the proposed LRTV method achieves the best performance. SSAHTV fails to restore most of the stripes. Meanwhile, the restoration result of SSAHTV is also oversmoothed, and most of the details are lost. LRMR also fails to restore some stripes. This is mainly because these stripes exist in the same place in most of the noisy HSI bands and are treated as the low-rank clean image in the LRMR processing. The proposed LRTV method achieves the best results in stripe and deadline removal.

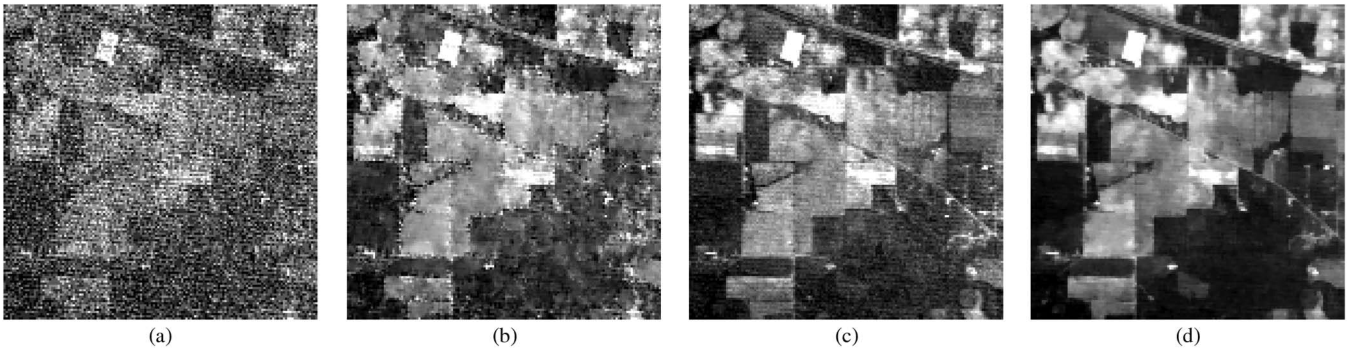
(a) (b) (c) (d)

Fig. 10. Restoration results of band 1 in real data experiment 2. (a) Original. (b) SSAHTV. (c) LRMR. (d) LRTV.

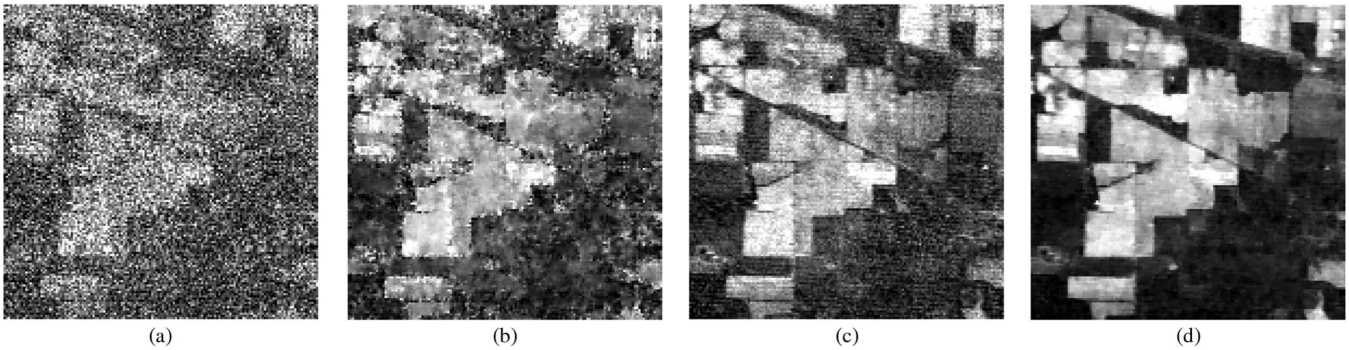
(a) (b) (c) (d)

Fig. 11. Restoration results of band 220 in real data experiment 2. (a) Original. (b) SSAHTV. (c) LRMR. (d) LRTV.

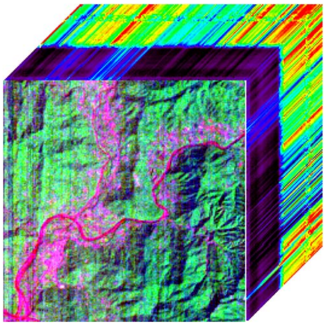

Fig. 12. EO-1 Hyperion data set used in real data experiment 3.

At the same time, the details are also preserved, as presented in Figs. 13(d) and 14(d).

We also present the vertical mean profiles of band 165 before and after restoration. The rapid fluctuations in Fig. 15(a) suggest the existence of stripes and deadlines in band 1. Here, it can again be clearly observed that the LRTV restoration method gives the best result among all the restored vertical mean profiles.

C. Discussion

In all the experiments with the LRTV method, we set the TV regularization parameter and the sparsity regularization parameter as $\tau = 10^{-2}$ and $\lambda = 1/\sqrt{MN}$, respectively, and used HySime to estimate the desired rank. In this part, we explain the reasons for choosing these parameter settings, and we present the convergence of the LRTV solver with the tested data set. All the experiments were based on the simulated data experiment in Case 2.

1) Sensitivity Analysis of Parameter τ: In the LRTV solver, parameter τ is adopted to control the tradeoff between the low-rank constraint and the TV regularization. When τ is larger, the power of the TV regularization is stronger, and vice versa. When τ is set to zero, the LRTV solver reduces to low-rank matrix factorization optimization. Fig. 16 presents the MPSNR and MSSIM values with the change of parameter τ. τ was selected from the set of [0, 0.001, 0.004, 0.007, 0.01, 0.02, 0.04, 0.07,

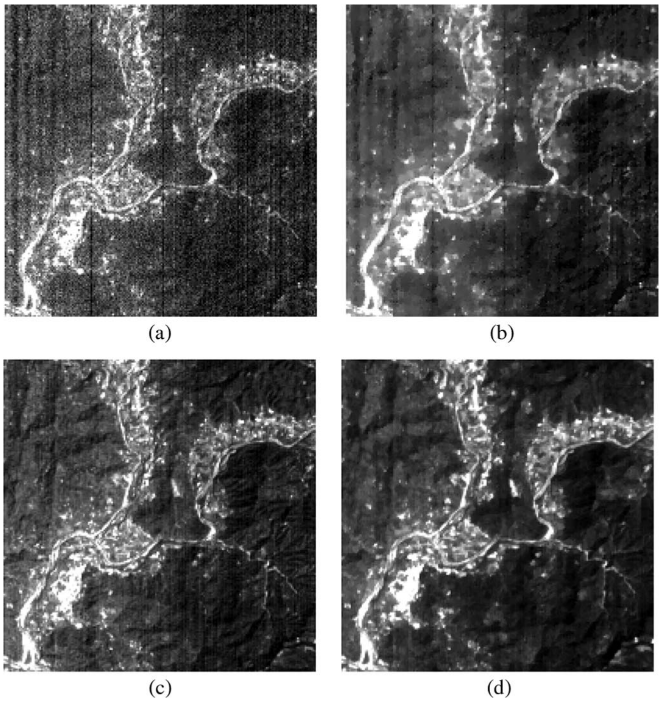
(a) (b) (c) (d)

Fig. 13. Restoration results of band 1 in real data experiment 3. (a) Original. (b) SSAHTV. (c) LRMR. (d) LRTV.

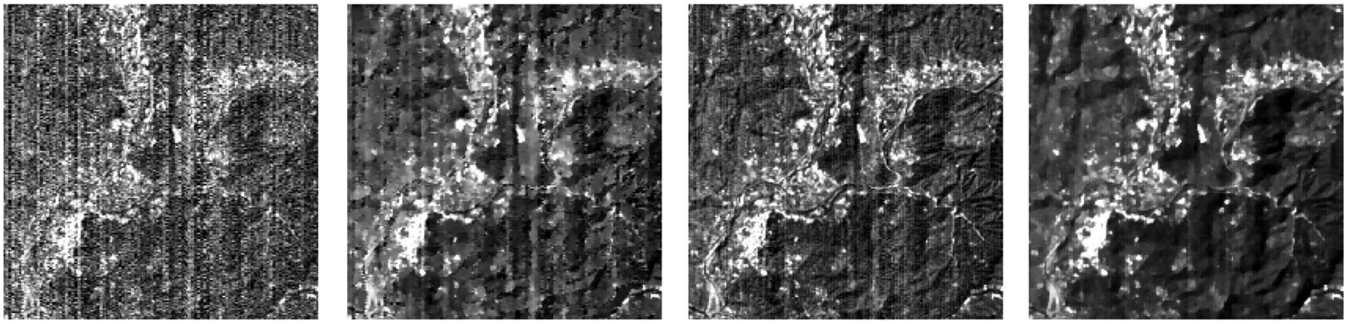
(a) (b) (c) (d)

Fig. 14. Restoration results of band 165 in real data experiment 3. (a) Original. (b) SSAHTV. (c) LRMR. (d) LRTV.

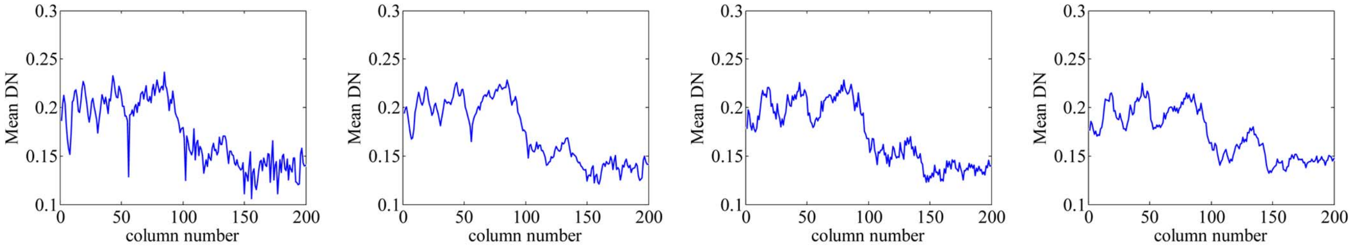

(a) (b) (c) (d)

Fig. 15. Vertical mean profiles of band 1 in the real data experiment 3. (a) Original. (b) SSAHTV. (c) LRMR. (d) LRTV.

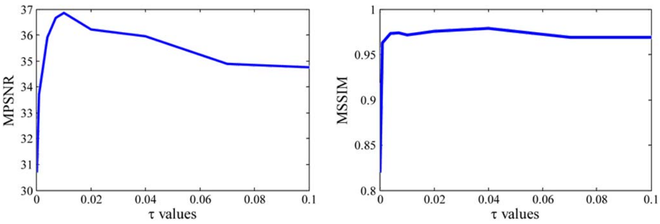

(a) (b)

Fig. 16. Sensitivity analysis of parameter τ (τ from 0 to 0.1). (a) Change in the MPSNR value. (b) Change in the MSSIM value.

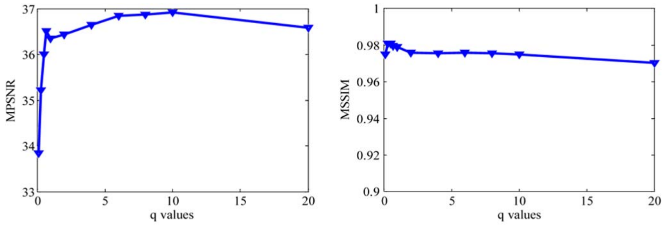

(a) (b)

Fig. 17. Sensitivity analysis of parameter λ (q from 0.1 to 20 with $\lambda = q/\sqrt{MN}$). (a) Change in the MPSNR value. (b) Change in the MSSIM value.

0.1]. In Fig. 16, it can be observed that, when $\tau = 0$, the MPSNR and MSSIM values are lower than the case of $\tau > 0$. This indicates the positive function of the TV regularization. When τ grows close to 0.01, the LRTV solver obtains the highest MPSNR and MSSIM values.

2) Sensitivity Analysis of Parameter λ: In the LRTV solver, λ is the parameter used to restrict the sparsity of the sparse noise. As in the RPCA model presented in [23], the sparsity regularization parameter was set to $\lambda = 1/\sqrt{MN}$, which was enough to guarantee the existence of an optimal solution. In the LRTV solver, this sparsity regularization parameter was also set to $\lambda = 1/\sqrt{MN}$. In Fig. 17, we set $\lambda = q/\sqrt{MN}$ and changed

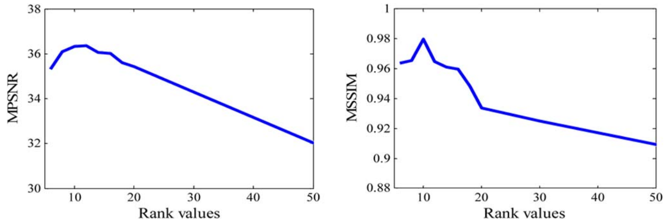

(a) (b)

Fig. 18. Sensitivity analysis of the rank constraint (rank estimated from 6 to 50). (a) Change in the MPSNR value. (b) Change in the MSSIM value.

q from the set of [0.1, 0.3, 0.5, 0.7, 1, 2, 4, 6, 8, 10, 20]. From the figure, it can be observed that the results of the LRTV solver are relatively stable, in both MPSNR and MSSIM values, when q was changed from 0.7 to 20. Therefore, we did not tune parameter λ, but we adopted the default value, as analyzed in [23].

3) Effectiveness of the Rank Constraint: In the LRTV optimization (19), although the nuclear norm is a slack operator of the rank minimization, we also add the rank constraint to the clean image. Compared to the RPCA model, the rank of the output clean image is sensitive to the TV regularization. Fig. 18 presents the MPSNR and MSSIM values of the LRTV solver with different rank-constrained values. In Fig. 18, it can be observed that the MPSNR and MSSIM values first grow and then drop with the growth in the estimated rank value. In addition, when the estimated rank was set to 224 (row numbers of X), the low-rank constraint was severely weakened and the LRTV solver reduces to the band-by-band TV restoration method. In another aspect, the LRTV solver achieved comparable results, when the estimated rank was set to close to the number of endmembers. This inspired us to use the HSI subspace estimation method (e.g., HySime) to estimate the desired rank value.

4) Convergence of the LRTV Solver: Fig. 19 presents the MPSNR and MSSIM gains versus the iteration number of the

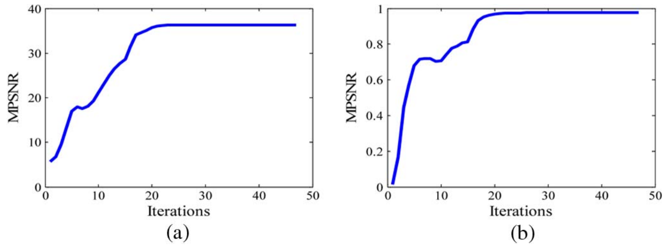

(a) (b)

Fig. 19. MPSNR and MSSIM values versus the iteration number of the LRTV solver. (a) MPSNR values of each iteration in Case 2 for the simulated data. (b) MSSIM values.

LRTV solver in Case 2 of the simulated experiment. Here, we can observe that, as the iteration progresses, the MPSNR and MSSIM values of the proposed method converge. This illustrates the convergent behavior of the proposed method with the tested data set.

V. CONCLUSION

In this paper, we have proposed a LRTV method for HSI mixed-noise removal. In the LRTV model, the low-rank constraint is utilized to effectively remove the sparse noise, by exploring the spectral similarity. Meanwhile, the TV regularization is adopted to preserve the local details and to further remove the Gaussian noise, by exploiting the spatial structure information. The low-rank constraint and the TV regularization are integrated into a unified framework and complement each other. The low-rank and sparse matrix decomposition can provide the sparse noise components for the TV regularization denoising. With the sparse noise information confirmed, the TV regularization can provide an enhanced clean image, and in return helps with the separation of the low-rank and sparse matrices. Furthermore, to tradeoff the low-rank constraint and the TV regularization, and to further remove the Gaussian noise of the HSI, a rank constraint, which denotes the number of endmembers, is added to the clean image. The proposed method was compared with other state-of-the-art restoration methods in several experiments, where LRTV performed best, in both visual and quantitative assessments.

Despite the good performance of the LRTV solver, it does have some room for further improvement. In the experiments, we added the same value of parameter to all the bands of the HSI. However, as introduced in [19], the noise intensity of different bands should be different. That is, a noise-adjusted TV regularization combined with a low-rank constraint will be studied in the future.

REFERENCES

[1] H. Zhang, J. Li, Y. Huang, and L. Zhang, "A nonlocal weighted joint sparse representation classification method for hyperspectral imagery," *IEEE J. Sel. Topics Appl. Earth Obs. Remote Sens.*, vol. 7, no. 6, pp. 2056–2065, Jun. 2014.

[2] Y. Qian, S. Jia, J. Zhou, and A. Robles-Kelly, "Hyperspectral unmixing via $L_{1/2}$ sparsity-constrained nonnegative matrix factorization," *IEEE Trans. Geosci. Remote Sens.*, vol. 49, no. 11, pp. 4282–4297, Nov. 2011.

[3] J. M. Bioucas-Dias *et al.*, "Hyperspectral unmixing overview: Geometrical, statistical, and sparse regression-based approaches," *IEEE J. Sel. Topics Appl. Earth Obs. Remote Sens.*, vol. 5, no. 2, pp. 354–379, Apr. 2012.

[4] D. W. Stein *et al.*, "Anomaly detection from hyperspectral imagery," *IEEE Signal Process. Mag.*, vol. 19, no. 1, pp. 58–69, Jan. 2002.

[5] M. Elad and M. Aharon, "Image denoising via sparse and redundant representations over learned dictionaries," *IEEE Trans. Image Process.*, vol. 15, no. 12, pp. 3736–3745, Dec. 2006.

[6] K. Dabov, A. Foi, V. Katkovnik, and K. Egiazarian, "Image denoising by sparse 3-D transform-domain collaborative filtering," *IEEE Trans. Image Process.*, vol. 16, no. 8, pp. 2080–2095, Aug. 2007.

[7] A. A. Green, M. Berman, P. Switzer, and M. D. Craig, "A transformation for ordering multispectral data in terms of image quality with implications for noise removal," *IEEE Trans. Geosci. Remote Sens.*, vol. 26, no. 1, pp. 65–74, Jan. 1988.

[8] H. Othman and S.-E. Qian, "Noise reduction of hyperspectral imagery using hybrid spatial-spectral derivative-domain wavelet shrinkage," *IEEE Trans. Geosci. Remote Sens.*, vol. 44, no. 2, pp. 397–408, Feb. 2006.

[9] D. Letexier and S. Bourennane, "Noise removal from hyperspectral images by multidimensional filtering," *IEEE Trans. Geosci. Remote Sens.*, vol. 46, no. 7, pp. 2061–2069, Jun. 2008.

[10] X. Liu, S. Bourennane, and C. Fossati, "Nonwhite noise reduction in hyperspectral images," *IEEE Geosci. Remote Sens. Lett.*, vol. 9, no. 3, pp. 368–372, May 2012.

[11] X. Guo, X. Huang, L. Zhang, and L. Zhang, "Hyperspectral image noise reduction based on rank-1 tensor decomposition," *ISPRS J. Photogramm. Remote Sens.*, vol. 83, pp. 50–63, Sep. 2013.

[12] Y. Qian and M. Ye, "Hyperspectral imagery restoration using nonlocal spectral spatial structured sparse representation with noise estimation," *IEEE J. Sel. Topics Appl. Earth Obs. Remote Sens.*, vol. 6, no. 2, pp. 499–515, Apr. 2013.

[13] S. Osher, M. Burger, D. Goldfarb, J. Xu, and W. Yin, "An iterative regularization method for total variation-based image restoration," *Multiscale Model. Simul.*, vol. 4, no. 2, pp. 460–489, Jun. 2005.

[14] M.-D. Iordache, J. M. Bioucas-Dias, and A. Plaza, "Sparse unmixing of hyperspectral data," *IEEE Trans. Geosci. Remote Sens.*, vol. 49, no. 6, pp. 2014–2039, Jun. 2011.

[15] H. Zhang, H. Shen, and L. Zhang, "A super-resolution reconstruction algorithm for hyperspectral images," *Signal Process.*, vol. 92, no. 9, pp. 2082–2096, Sep. 2012.

[16] D. Needell and R. Ward, "Stable image reconstruction using total variation minimization," *SIAM J. Imag. Sci.*, vol. 6, no. 2, pp. 1035–1058, Mar. 2013.

[17] H. Zhang, "Hyperspectral image denoising with cubic total variation model," *ISPRS Ann. Photogramm. Remote Sens. Spat. Inf. Sci.*, vol. I-7, pp. 95–98, Jul. 2012.

[18] S. K. Kuiteing, G. Coluccia, A. Barducci, M. Barni, and E. Magli, "Compressive hyperspectral imaging using progressive total variation," in *Proc. IEEE ICASSP*, 2014, pp. 7794–7798.

[19] Q. Yuan, L. Zhang, and H. Shen, "Hyperspectral image denoising employing a spectral spatial adaptive total variation model," *IEEE Trans. Geosci. Remote Sens.*, vol. 50, no. 10, pp. 3660–3677, Oct. 2012.

[20] L. Ma, J. Yu, and T. Zeng, "Sparse representation prior and total variation—Based image deblurring under impulse noise," *SIAM J. Imag. Sci.*, vol. 6, no. 4, pp. 2258–2284, 2013.

[21] J.-F. Cai, R. H. Chan, and M. Nikolova, "Two-phase approach for deblurring images corrupted by impulse plus Gaussian noise," *Inverse Problems Imag.*, vol. 2, no. 2, pp. 187–204, 2008.

[22] Q. Li, H. Li, Z. Lu, Q. Lu, and W. Li, "Denoising of hyperspectral images employing two-phase matrix decomposition," *IEEE J. Sel. Topics Appl. Earth Obs. Remote Sens.*, vol. 7, no. 9, pp. 3742–3754, Sep. 2014.

[23] E. J. Candès, X. Li, Y. Ma, and J. Wright, "Robust principal component analysis?" *J. ACM*, vol. 58, no. 3, May 2011.

[24] N. Wang, T. Yao, J. Wang, and D.-Y. Yeung, "A probabilistic approach to robust matrix factorization," in *Computer Vision-ECCV*. Berlin, Germany: Springer-Verlag, 2012, pp. 126–139.

[25] Y. Wang, A. Szlam, and G. Lerman, "Robust locally linear analysis with applications to image denoising and blind inpainting," *SIAM J. Imag. Sci.*, vol. 6, no. 1, pp. 526–562, 2013.

[26] C.-I. Chang and Q. Du, "Interference and noise-adjusted principal components analysis," *IEEE Trans. Geosci. Remote Sens.*, vol. 37, no. 5, pp. 2387–2396, Sep. 1999.

[27] H. Zhang, W. He, L. Zhang, H. Shen, and Q. Yuan, "Hyperspectral image restoration using low-rank matrix recovery," *IEEE Trans. Geosci. Remote Sens.*, vol. 52, no. 8, pp. 4729–4743, Aug. 2014.

[28] T. Hu, H. Zhang, H. Shen, and L. Zhang, "Robust registration by rank minimization for multiangle hyper/multispectral remotely sensed imagery," *IEEE J. Sel. Topics Appl. Earth Obs. Remote Sens.*, vol. 7, no. 6, pp. 2443–2457, Jun. 2014.

[29] R. Zhu, M. Dong, and J. Xue, "Spectral nonlocal restoration of hyperspectral images with low-rank property," *IEEE J. Sel. Topics Appl. Earth Obs. Remote Sens.*, to be published, DOI: 10.1109/JSTARS.2014.2370062.

[30] W. He, H. Zhang, L. Zhang, and H. Shen, "Hyperspectral image denoising via noise-adjusted iterative low-rank matrix approximation," *IEEE J. Sel. Topics Appl. Earth Obs. Remote Sens.*, to be published.

[31] W. He, H. Zhang, L. Zhang, and H. Shen, "A noise-adjusted iterative randomized singular value decomposition method for hyperspectral image denoising," in *Proc. IEEE IGARSS*, Quebec, ON, Canada, 2014, pp. 1536–1539.

[32] G. Chen and S.-E. Qian, "Denoising of hyperspectral imagery using principal component analysis and wavelet shrinkage," *IEEE Trans. Geosci. Remote Sens.*, vol. 49, no. 3, pp. 973–980, Mar. 2011.

[33] Y. Q. Zhao and J. Yang, "Hyperspectral image denoising via sparse representation and low-rank constraint," *IEEE Trans. Geosci. Remote Sens.*, vol. 53, no. 1, pp. 296–308, Jan. 2015.

[34] M. Golbabaee and P. Vandergheynst, "Joint trace/TV norm minimization: A new efficient approach for spectral compressive imaging," in *Proc. 19th IEEE ICIP*, 2012, pp. 933–936.

[35] X. He, L. Condat, J. M. Bioucas-Dias, J. Chanussot, and J. Xia, "A new pansharpening method based on spatial and spectral sparsity priors," *IEEE Trans. Image Process.*, vol. 23, no. 9, pp. 4160–4174, Sep. 2014.

[36] Z. Lin, M. Chen, and Y. Ma, "The augmented Lagrange multiplier method for exact recovery of corrupted low-rank matrices," Univ. of Illinois at Urbana-Champaign, Champaign, IL, USA, Tech. Rep. UILU-ENG-09-2215, 2009.

[37] G. Liu *et al.*, "Robust recovery of subspace structures by low-rank representation," *IEEE Trans. Pattern Anal. Mach. Intell.*, vol. 35, no. 1, pp. 171–184, Jan. 2013.

[38] M. D. Iordache, J. M. Bioucas-Dias, and A. Plaza, "Total variation spatial regularization for sparse hyperspectral unmixing," *IEEE Trans. Geosci. Remote Sens.*, vol. 50, no. 11, pp. 4484–4502, Nov. 2012.

[39] L. I. Rudin, S. Osher, and E. Fatemi, "Nonlinear total variation based noise removal algorithms," *Phys. D, Nonlinear Phenom.*, vol. 60, no. 1–4, pp. 259–268, Nov. 1992.

[40] A. Beck and M. Teboulle, "Fast gradient-based algorithms for constrained total variation image denoising and deblurring problems," *IEEE Trans. Image Process.*, vol. 18, no. 11, pp. 2419–2434, Nov. 2009.

[41] A. Mnih and R. Salakhutdinov, "Probabilistic matrix factorization," in *Proc. Adv. Neural Inf. Process. Syst.*, 2007, pp. 1257–1264.

[42] X. Ding, L. He, and L. Carin, "Bayesian robust principal component analysis," *IEEE Trans. Image Process.*, vol. 20, no. 12, pp. 3419–3430, Dec. 2011.

[43] R. Mazumder, T. Hastie, and R. Tibshirani, "Spectral regularization algorithms for learning large incomplete matrices," *J. Mach. Learn. Res.*, vol. 11, pp. 2287–2322, 2010.

[44] V. Chandrasekaran, S. Sanghavi, P. A. Parrilo, and A. S. Willsky, "Rank-sparsity incoherence for matrix decomposition," *SIAM J. Optim.*, vol. 21, no. 2, pp. 572–596, Jun. 2011.

[45] J.-F. Cai, E. J. Candès, and Z. Shen, "A singular value thresholding algorithm for matrix completion," *SIAM J. Optim.*, vol. 20, no. 4, pp. 1956–1982, Jan. 2010.

[46] D. P. Bertsekas, *Constrained Optimization and Lagrange Multiplier Methods*. New York, NY, USA: Academic, 2014.

[47] J. M. Bioucas-Dias and J. M. Nascimento, "Hyperspectral subspace identification," *IEEE Trans. Geosci. Remote Sens.*, vol. 46, no. 8, pp. 2435–2445, Aug. 2008.

[48] [Online]. Available: https://engineering.purdue.edu/~biehl/MultiSpec/hyperspectral.html

[49] [Online]. Available: http://speclab.cr.usgs.gov/spectral.lib

[50] Z. Wang, A. C. Bovik, H. R. Sheikh, and E. P. Simoncelli, "Image quality assessment: From error visibility to structural similarity," *IEEE Trans. Image Process.*, vol. 13, no. 4, pp. 600–612, Apr. 2004.

[51] [Online]. Available: http://www.tec.army.mil/hypercube

[52] [Online]. Available: http://www.gscloud.cn/

Wei He (S'14) received the B.S. degree from the School of Mathematics and Statistics from Wuhan University, Wuhan, China, in 2012. He is currently working toward the Ph.D. degree with the State Key Laboratory of Information Engineering in Surveying, Mapping, and Remote Sensing, Wuhan University, Wuhan, China.

His research interests include image quality improvement, remote sensing image processing, and low-rank representation.

Hongyan Zhang (M'13) received the B.S. degree in geographic information system and the Ph.D. degree in photogrammetry and remote sensing from Wuhan University, Wuhan, China, in 2005 and 2010, respectively.

He is currently an Associate Professor with the State Key Laboratory of Information Engineering in Surveying, Mapping, and Remote Sensing, Wuhan University. He has published more than 30 research papers. His current research interests focus on image reconstruction, hyperspectral image processing, sparse representation, and low-rank methods for sensing image imagery.

Dr. Zhang serves as a reviewer for about ten international academic journals.

Liangpei Zhang (M'06–SM'08) received the B.S. degree in physics from Hunan Normal University, Changsha, China, in 1982, the M.S. degree in optics from the Xi'an Institute of Optics and Precision Mechanics of Chinese Academy of Sciences, Xi'an, China, in 1988, and the Ph.D. degree in photogrammetry and remote sensing from Wuhan University, Wuhan, China, in 1998.

He is currently the Head of the Remote Sensing Division, State Key Laboratory of Information Engineering in Surveying, Mapping, and Remote Sensing, Wuhan University. He is also a Chang Jiang Scholar Chair Professor appointed by the Ministry of Education of China. He is currently a Principal Scientist for the China State Key Basic Research Project (2011–2016) appointed by the Ministry of National Science and Technology of China to lead the remote sensing program in China. He has more than 410 research papers. He is the holder of 15 patents. His research interests include hyperspectral remote sensing, high-resolution remote sensing, image processing, and artificial intelligence.

Dr. Zhang is a Fellow of the Institution of Engineering and Technology, an Executive Member (Board of Governor) of the China National Committee of the International Geosphere-Biosphere Programme, and an Executive Member of the China Society of Image and Graphics. He was a recipient of the 2010 Best Paper Boeing Award and the 2013 Best Paper ERDAS Award from the American Society of Photogrammetry and Remote Sensing (ASPRS). He regularly serves as a Cochair of the series SPIE Conferences on Multispectral Image Processing and Pattern Recognition, Conference on Asia Remote Sensing, and many other conferences. He edits several conference proceedings, issues, and geoinformatics symposiums. He also serves as an Associate Editor for the *International Journal of Ambient Computing and Intelligence*, the *International Journal of Image and Graphics*, the *International Journal of Digital Multimedia Broadcasting*, the *Journal of Geo-Spatial Information Science*, the *Journal of Remote Sensing*, and the IEEE TRANSACTIONS ON GEOSCIENCE AND REMOTE SENSING.

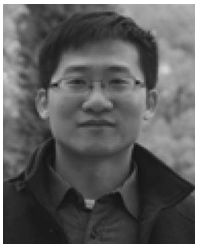

Huanfeng Shen (M'11–SM'13) received the B.S. degree in surveying and mapping engineering and the Ph.D. degree in photogrammetry and remote sensing from Wuhan University, Wuhan, China, in 2002 and 2007, respectively.

In July 2007, he joined the School of Resource and Environmental Sciences, Wuhan University, where he has been a Luojia Distinguished Professor. He has published more than 100 research papers. His research interests include image quality improvement, remote sensing mapping and application, data fusion and assimilation, and regional and global environmental change.

Dr. Shen is a Council Member of the China Association of Remote Sensing Application. He is currently a member of the Editorial Board of the *Journal of Applied Remote Sensing*. He has been supported by several talent programs, such as the China National Science Fund for Excellent Young Scholars (2014), the New Century Excellent Talents by the Ministry of Education of China (2011), and the Hubei Science Fund for Distinguished Young Scholars (2011).